MATERIALS CHEMISTRY FRONTIERS

RESEARCH ARTICLE

View Article Online
View Journal | View Issue

Cite this: *Mater. Chem. Front.*, 2022, **6**, 737

Layered tungsten-based composites and their pseudocapacitive and electrocatalytic performance†

Oluwafunmilola Ola, *[a] Kunyapat Thummavichai,[b] Yu Chen,[bc] Nannan Wang,[b] Qijian Niu,[d] Jiaao Wang,[e] Shibin Sun[f] and Yanqiu Zhu[b]

Received 5th May 2021,
Accepted 26th January 2022

DOI: 10.1039/d1qm00678a

rsc.li/frontiers-materials

With the rapid development of heterostructured electrocatalysts, the potential application of transition metal dichalcogenide (TMD)-based composites for electrocatalysis have attracted intense attraction owing to their unique optical, electronic, and mechanical properties. Herein, a facile solvothermal method to obtain heterostructured composites consisting of TMD (WS_2) and graphitic carbon nitride ($g\text{-}C_3N_4$) is reported. DFT calculation results demonstrates that the interface interaction between $g\text{-}C_3N_4$ and WS_2 optimizes the electronic structure of composite materials and activates the active sites. The WS_2–$g\text{-}C_3N_4$ composites with surface sulfur and nitrogen vacancies exhibit high specific capacitance of 1156 F g^{-1} and excellent cycling stability with no capacitance loss over 2000 charge–discharge cycles, demonstrating huge potential in applications for pseudocapacitive energy storage. In addition, WS_2–$g\text{-}C_3N_4$ composites can attain excellent hydrogen production activity to reach a current density of 10 mA cm^{-2} at an overpotential of −0.170 V (*vs.* RHE) and Tafel slope of 59 mV dec^{-1}. This work provides an effective way for the synthesis of heterostructured electrocatalysts with efficient activity for energy conversion and storage.

1. Introduction

Two-dimensional (2D) layered transition metal dichalcogenides (TMDs) have emerged as a promising class of catalysts due to their unique crystal structure and layer-dependent optoelectronic properties which offer great prospects for exploitation in applications ranging from photovoltaics, photocatalysis to electrocatalysis. Among TMDs, tungsten and its compounds (*i.e.*, WS_x) have been tested as electrocatalysts in their intrinsic or hybrid form, because of their polymorphic nature and ability to participate in complex interatomic interactions with other materials *via* surface engineering. The structural features of WS_x, such as their lateral size, layer number and active sites *i.e.* step edges and atomic vacancies, have been shown to greatly influence their electrocatalytic properties and performance.[1] When the lateral size of WS_x is reduced within the nanoscale domain, unique mechanical and optoelectronic properties arising from quantum confinement effects have been observed.[2] Their individual sandwich layers made up of transition metal and chalcogen bound by weak van der Waals forces can also offer large surface area and permeable channels for ion adsorption and transport.[3]

Experimental and computational studies have established that exposed chalcogen edge sites of WS_x can facilitate improved electrocatalytic performance while the basal surfaces remain catalytically inert.[3,4] Accordingly, WS_x can be supported on carbon nanostructures to increase the activity of the inert basal surface of TMD through increased defect sites created *via* the preferential bonding between the basal planes of WS_x and carbon surfaces. Carbon nanostructures can also serve as conductive supports to further augment the electrical conductivity while increasing contact resistance. Pure carbon and hybrids of graphitic carbon nitride ($g\text{-}C_3N_4$) have been reported to hold great promise as alternatives to expensive precious metal-based

[a] *Faculty of Engineering, The University of Nottingham, University Park, Nottingham, NG7 2RD, UK. E-mail: Oluwafunmilola.Ola1@nottingham.ac.uk; Tel: +44 1157 487264*
[b] *Guangxi Institute Fullerene Technology (GIFT), Key Laboratory of New Processing Technology for Nonferrous Metals and Materials, Ministry of Education, School of Resources, Environment and Materials, Guangxi University, Nanning, 530004, China*
[c] *College of Engineering, Mathematics and Physical Sciences, University of Exeter, EX4 4QF, UK*
[d] *School of Agricultural Equipment Engineering, Jiangsu University, Zhenjiang, Jiangsu, 212013, China*
[e] *School of Material Science and Engineering, University of Jinan, Jinan, 250022, China*
[f] *College of Logistics Engineering, Shanghai Maritime University, Shanghai 201306, China*

† Electronic supplementary information (ESI) available. See DOI: 10.1039/d1qm00678a

catalysts for water splitting and CO_2 reduction due to their tunable chemistry, high thermal and chemical stability, low cost, and non-toxicity.[5,6]

Several strategies have been developed to tailor the structural features of g-C_3N_4 to enhance their electrochemical activity and durability. Improvements in electronic structure and energy band configuration of g-C_3N_4 based nanocomposites have been demonstrated by the functionalization of g-C_3N_4 at atomic and molecular levels *via* elemental doping and copolymerization, respectively. The content of heteroatomic species of nitrogen and sulfur are particularly useful for modifying surface functional groups and crystallinity which can increase charge carrier mobility with low diffusion barriers during cycling to enhance rate capability and electrochemical performance. For example, quaternary nitrogen has been reported to improve electrical conductivity which facilitates the charge/discharge process while pyrrolic and pyridinic nitrogen can introduce active sites and defects.[7,8] Surface sulfur vacancies have been reported to alter the electronic structure of host materials by reducing the electron transition energy barrier and enhancing electrophilic adsorption.[9] Other ways of improving the physicochemical properties of g-C_3N_4 for target-specific applications include coupling with other semiconductors, metal/metal oxides as a cocatalyst or incorporation of carbonaceous materials to form hybrid nanocomposites. Since g-C_3N_4 possesses an analogous layered structure with finite exposed edges, the fabrication of an organic/inorganic hybrid nanocomposites with another layered material such as WS_2 can lead to the formation of surface heterojunctions for efficient charge collection and separation while exposing active sites required for electrocatalytic reactions. Understanding the effect of growing WS_2 on a g-C_3N_4 based support for electrocatalytic reactions is crucial, and yet remains to be explored.

Herein, we report the formulation of tungsten-based composites *via* the growth of WS_2 on an interconnected, macroscopic g-C_3N_4 scaffold using $W_{18}O_{49}$ derived from solvothermal treatment as a template. The presence of different heteroatomic surface species of nitrogen and sulfur were found to influence the rate capability and cyclic performance of the tungsten-based composites. DFT calculations confirm the importance of WS_2–g-C_3N_4 heterostructure design. Benefitting from optimal specific surface area and nitrogen and sulfur content of 11 at% and 1.01 at%, respectively, the WS_600 composite exhibits high specific capacitance of 1156 F g^{-1} and excellent cycling stability with no capacitance loss over 2000 charge–discharge cycles, demonstrating huge potential in applications for pseudocapacitive energy storage. In addition, the WS_600 composite can attain excellent hydrogen production activity to reach a current density of 10 mA cm^{-2} at an overpotential of −0.170 V and Tafel slope of 59 mV dec^{-1}.

2. Experimental

2.1. Preparation of WS_2–g-C_3N_4 composites

The scheme for fabricating the WS_2–g-C_3N_4 composites is illustrated in Fig. 1. All chemical compounds and solvents used during synthesis were purchased from Sigma Aldrich. Solvothermal treatment, an easy and low-cost methodology, was employed to grow $W_{18}O_{49}$ on melamine ($C_3H_6N_6$) scaffold using the tungsten hexachloride (WCl_6, 0.075 g) – cyclohexanol ($C_6H_{12}O$, 50 mL) mixture, subjected to heat treatment for 6 h at 200 °C.[10]

Prior to sulfidation, the $W_{18}O_{49}$–$C_3H_6N_6$ composites were subjected to carbonization under argon atmosphere to yield $W_{18}O_{49}$–g-C_3N_4 composites at reaction temperatures of 400, 600 and 800 °C to derive samples, which were referred to as WS_400, WS_600 and WS_800, respectively. Once the reaction temperature mentioned above was attained, hydrogen sulfide gas was introduced into the reaction chamber for 50 min to initiate the sulfidation process for the samples. After sulfidation, most of the $W_{18}O_{49}$ grown on the g-C_3N_4 scaffolds were converted into WS_2, depending on the reaction temperature.

2.2. Materials characterization and electrochemical testing

The crystalline structure of the composites was characterized by X-ray diffraction (XRD) using a Bruker D8 Advance diffractometer (operated at 40 kV, 40 mA), with a Cu Kα radiation, at a step size of 0.02° and a dwell time of 1 s. The Raman spectra were acquired at room temperature using a Renishaw benchtop system, with 532 nm excitation wavelength and 2400 l mm^{-1} grating. Surface chemical analysis was performed on a Kratos Axis Ultra system with a monochromated Al Kr X-ray source

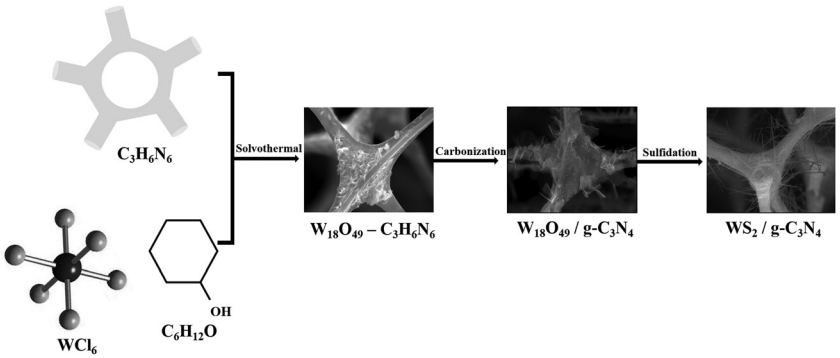

Fig. 1 Schematic of synthetic procedure for WS_2–g-C_3N_4 composites.

operated at 10 mA emission current and 15 kV anode potential. Scanning electron microscopy (SEM), transmission electron microscopy (TEM), Raman spectroscopy, X-ray diffraction (XRD) and X-ray photoelectron spectroscopy (XPS) were used to conduct the morphological and structural analyses. Elemental composition of WS_2–g-C_3N_4 composites was evaluated using scanning electron microscopy (Hitachi S3200N, Oxford instrument – SEM-EDS) and high-resolution transmission electron microscopy (JEOL-2100, HR-TEM), respectively. The Brunauer–Emmett–Teller (BET) surface areas and pore size distribution of the WS_2/g-C_3N_4 composites were measured with the Micromeritics ASAP 2020 nitrogen adsorption analyzer.

2.3. Electrochemical measurements

Electrochemical measurements for hydrogen evolution reaction (HER) and capacitance were performed at room temperature using a CHI-660E workstation coupled with a rotating disk electrode (RDE) system consisting of Ag/AgCl/KCl, platinum wire and glassy carbon rotating disk electrode (GCE) covered with catalyst ink as reference, counter and working electrodes, respectively. The working electrode was prepared by drop casting of catalyst ink prepared from a mixture of 5 μL of Nafion solution, 1 mL of ethanol/water solution and 3 mg of composite sample. The active mass loading of the electrodes was 0.21 mg cm^{-2}. For the HER, electrochemical measurements were carried out in a 0.5 M H_2SO_4 (Sigma Aldrich) electrolyte solution at different potentials and scan rates varying from 0 −0.8 V and 10–100 mV, respectively. The experimentally measured potential *versus* Ag/AgCl, $E_{Ag/AgCl}$, was calibrated with respect to the RHE (reversible hydrogen electrode), E_{RHE}, according to the Nernst equation; $E_{RHE} = E_{Ag/AgCl} + E^0_{Ag/AgCl} + 0.059$ pH (at 25 °C) where $E^0_{Ag/AgCl}$ = 0.1976 V at 25 °C. The acquired HER experimental values were generated in 0.5 M H_2SO_4 solution and corrected for iR loss. Chronoamperometric measurements were performed by applying the corresponding potential to support an initial current density of about 10 mA cm^{-2} for 10 h for the HER. Electrochemical impedance spectroscopy measurements were carried out after applying the AC voltage with 10 mV amplitude at a frequency range of 0.05 Hz to 10 kHz, using the open circuit potential.

For specific capacitance (C_{sp}), galvanostatic discharge/charge (GCD) measurements were recorded at current densities ranging from 2 to 15 A g^{-1}. Specific capacitance (C_{sp}) was derived from GCD measurements using the equation: $C_{sp} = I/m$ ($\Delta V/\Delta t$) where I (A) is the discharge current, Δt (s) is the discharge time consumed in the potential window *of* ΔV (V) and m represents the mass of active material. The stability of the supercapacitor was evaluated by cyclic GCD measurements at current density of 15 A g^{-1} for 10 000 cycles.

2.4. DFT Calculation parameters

In this work, the first-principles density functional theory (DFT) was applied by using the projector augmented wave method (PAW).[11] Additionally, the exchange–correlation function was approved by employing the Perdew–Burke–Ernzerhof generalized gradient approximation (PBE-GGA).[12] For the results, we applied the wave functions with plane-wave expansion with 400 eV cutting off energy while force tolerance was set at 0.05 eV $Å^{-1}$ for relaxation. Also, certain surfaces of the (100) planes were chosen to build the heterostructure of WS_2–g-C_3N_4 nanocomposites. Furthermore, the WS_2 surface of (100) with 7 × 7 units of and the g-C_3N_4 surface (100) with 3 × 3 units were established to simulate the heterostructure of WS_2–g-C_3N_4. Since HER consists of four elementary reactions, the electron transfer for each reaction was supplemented by the process of proton expulsion, which can be indicated below:

$$H_2 + * \rightarrow H^* + H^+ + e^-$$

$$H^* \rightarrow * + H^+ + e^-$$

where * and X* are demonstrated as an adsorption site and an adsorbed X intermediary on the reaction surface. The $H^+ + e^-$ can be shown as free energy of half formation energy of H_2 at 1 atm within 298 K. The reduction activity was calculated by using $\Delta G = \Delta E + \Delta ZPE - T\Delta S$ for the free energy where the ΔE was acquired by its geometric forms. Moreover, the ΔZPE and ΔS were defined by using the computational vibration frequency, combined with the standard tables of gas reactants. The entropy was assumed as zero at the adsorbed surface-active site.

3. Results and discussion

3.1. Structural and physicochemical properties

To investigate the structure–activity relationships, DFT calculations were applied to study the electronic structure of these catalysts. Here, g-C_3N_4, WS_2 and WS_2–g-C_3N_4 are considered as the model object to analyse the difference of electronic structure and catalytic mechanism. Density of states (DOS) and partial density of states (PDOS) of these materials are shown in Fig. 2.

The band gap of WS_2, g-C_3N_4, and WS_2–g-C_3N_4 are 1.63 eV, 1.21 eV, and 0.85 eV, respectively. The WS_2–g-C_3N_4 composite exhibits the lowest band gap energy, beneficial to electron transfer in catalytic process. Furthermore, atomic orbit such as N, S, and W of the WS_2–g-C_3N_4 composite is closer to the Fermi level compared with g-C_3N_4 and WS_2, which supports this finding. In addition, enhanced electron transfer at the interface of g-C_3N_4 and WS_2 can further facilitate the absorption of water molecules. Therefore, designing the heterostructure of WS_2–g-C_3N_4 has a positive effect for improving the catalytic activity of HER. To understand the catalytic process for HER reaction, the reaction energies of WS_2, g-C_3N_4, and WS_2–g-C_3N_4 at each step of the HER reaction are calculated. The Gibbs free energies of pristine g-C_3N_4, WS_2 and WS_2–g-C_3N_4 composite have been calculated to investigate HER activity (Fig. 3). As shown in Fig. 3, the Volmer–Heyrovsky reaction pathway of HER is that H^+ was first adsorbed onto the surface of solid catalysts, then formed in the intermediate species H*, finally converted into hydrogen.

In the Volmer–Heyrovsky reaction, the generation of intermediate species H* is the important rate determining step in

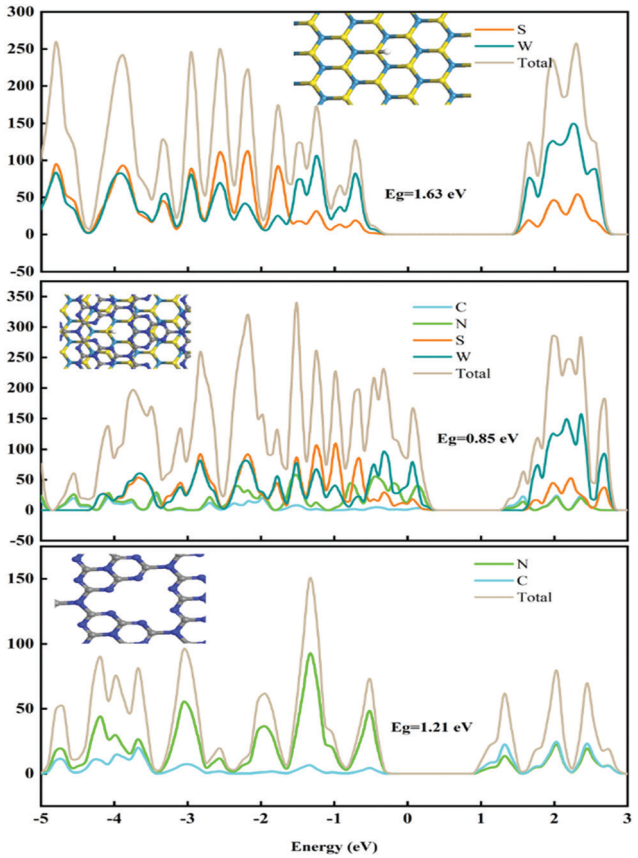

Fig. 2 Theoretical calculation of the density of states (DOSs) near the Fermi level.

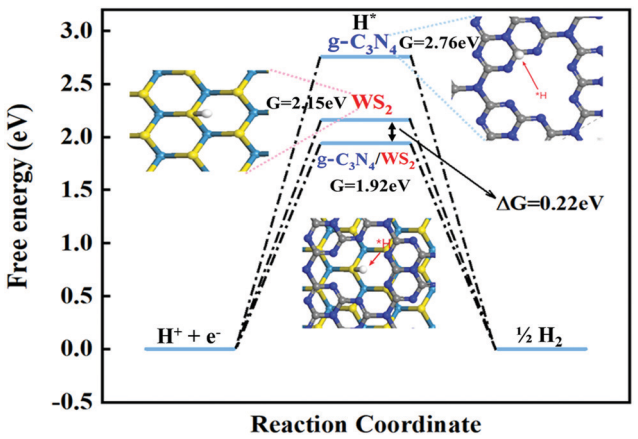

Fig. 3 Free-energy diagram for the HER with Volmer–Heyrovsky reactions on pristine g-C_3N_4, WS_2 and WS_2–g-C_3N_4 composite.

the HER reaction and needs to overcome some reaction energy barriers. Fig. 3 displays the calculated Gibbs free energy (ΔGH*) of hydrogen adsorption (0.2 2 eV) and the Gibbs free energy of C_3N_4, WS_2 and C_3N_4/WS_2, which are 2.76 eV, 2.14 eV and 1.92 eV, respectively, which is in line with previous reported values.[13] The WS_2–g-C_3N_4 composite shows the lowest activation barriers than those of WS_2 and g-C_3N_4, indicating that the WS_2–g-C_3N_4 possesses the highest electrocatalytic HER activity. Our calculation results also demonstrate that the interface interaction between g-C_3N_4 and WS_2 optimizes the electronic structure of composite materials *via* the promotion of more electrochemical active sites and improved charge transfer kinetics required for optimal electrochemical performance. These calculation results confirm the importance of WS_2–g-C_3N_4 heterostructure design.

As shown in Fig. 4a and Fig. S1 (ESI†), a sparse to dense mat of nanowires was grown on the g-C_3N_4 scaffolds when the calcination temperature increased from 400–800 °C, respectively. The average thickness and length of the nanowires were between 10–30 nm and ≤ 1 μm, respectively. Low- and high-resolution TEM images show homogeneous, layered, spindle-shaped structures of varying width and length stacked on top of each other in different directions (Fig. 4b). The interplanar spacing of the spindle shaped structures are 0.38, 0.32 and 0.27 nm which matched the d spacing values for (002), (002) and (100) planes of g-C_3N_4, orthorhombic (β) WO_3 and hexagonal WS_2, respectively.[14] The presence of WO_3 is due to the reaction of some $W_{18}O_{49}$ nanoparticles with residue oxygen during the reduction reaction in H_2S/Ar atmosphere between 400–800 °C. The phase transformation of $W_{18}O_{49}$ is expected to initially proceed through the formation of WS_3 *via* the substitution of oxygen atoms with sulphur atoms.[15] Further reaction leads to the formation of WS_2 with residual orthorhombic WO_3 nanoparticles due to oxidation occurring during sulfidation. The presence and homogeneous distribution of C, N, W, O and S was clearly confirmed from the elemental mapping of WS_800 (Fig. 4d–i) which is consistent with the XRD and XPS results, to be described below.

The XRD patterns of the as-synthesized WS_2–g-C_3N_4 composites prepared after thermal treatment at 400–800 °C are shown in Fig. 5a. Phase characterization indicates that the samples are crystalline and in good agreement with orthorhombic (β) WO_3 (JCPDS card no. 20-1324), g-C_3N_4 (JCPDS no. 87-1526), and hexagonal WS_2 (JCPDS card no. 08-0237). The diffraction peaks at 2θ = 32.8°, 33.6°, 35.3°, 55.9° and 57.6° are indexed to (100), (101), (102), (106) and (110) planes of hexagonal WS_2, respectively. The diffraction peak at 27.6° is attributed to the (002) plane of g-C_3N_4 linked to the interplanar stacking of conjugated aromatic systems.[16] The peaks of β-WO_3 and WS_2 become sharper with the increase of reaction temperatures. Raman spectra in Fig. 5b have revealed the characteristic peaks of the $W_{18}O_{49}$ and WS_2 in the 200–1000 cm^{-1} range and the D (1348 cm^{-1}) and G (1587 cm^{-1}) bands for g-C_3N_4 in the WS_2–g-C_3N_4 composites prepared at different temperatures. The peak intensity ratios of the disordered amorphous carbon (D band) to graphitic carbon (G band) are calculated to be 1.33, 1.23 and 1.07 for WS_400, WS_600 and WS_800, respectively. The absence of 2D band linked to the second-order two-phonon process of graphene and low degree of graphitization is ascribed to the presence of structural defects and high nitrogen content.

Only WS_400 presents a Raman band at 129 cm^{-1}, which is assigned to the β-WO_3 phase. This confirms that some oxidation reaction occurred during the growth of WS_2 on the g-C_3N_4

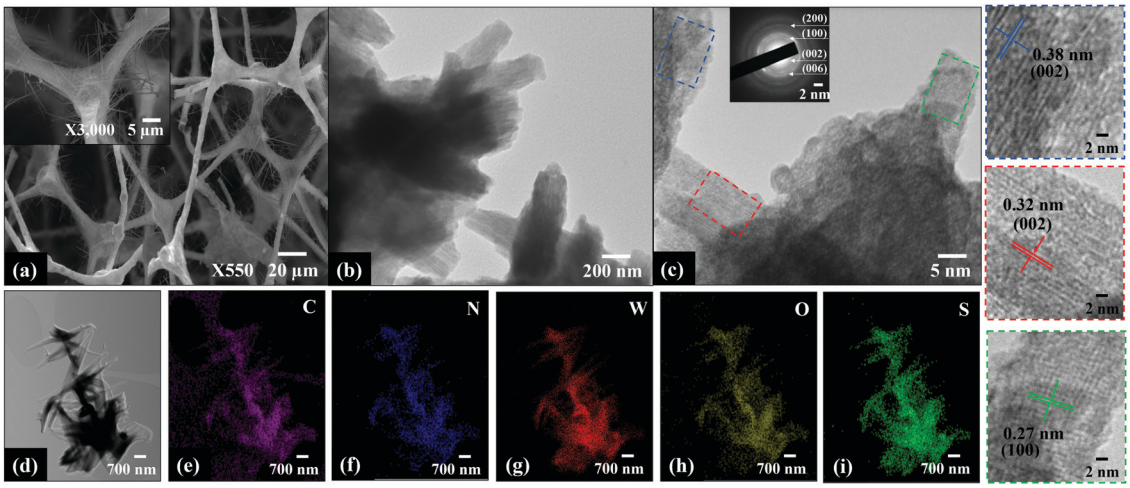

Fig. 4 (a) SEM image of WS_2–g-C_3N_4 composites prepared at 800 °C (WS_800), with inset high-resolution image showing the nanowire morphology of WS_800. TEM analysis of WS_800: (b) low magnification image, (c) high-resolution images showing lattice planes of g-C_3N_4, WO_3 and WS_2. (d–i) TEM images with corresponding elemental mapping of WS_800.

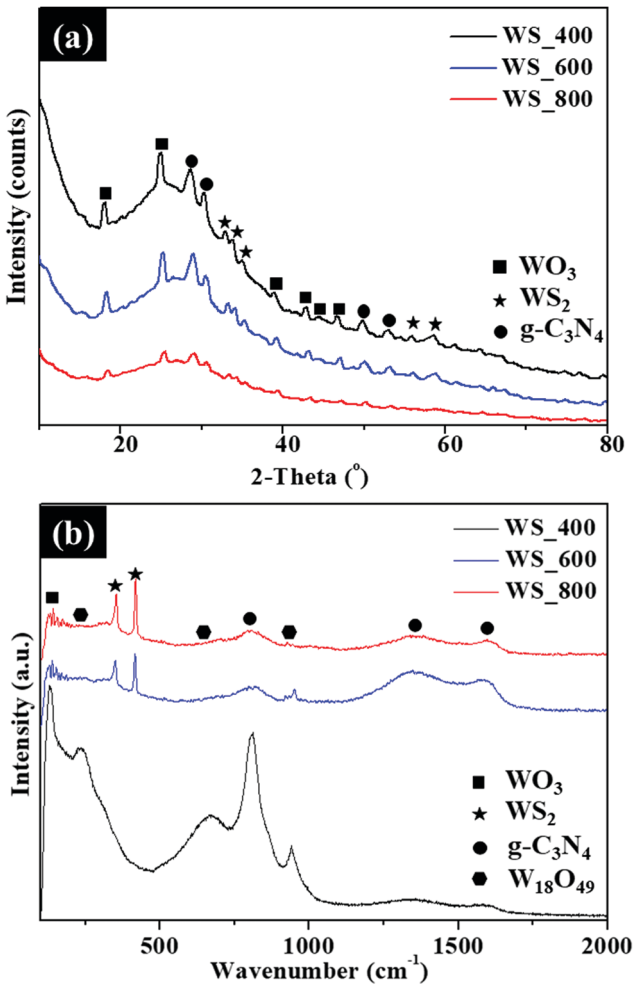

Fig. 5 (a) XRD patterns and (b) Raman spectra of the WS_2–g-C_3N_4 composites prepared at different temperatures.

scaffold. The 226 cm^{-1} band could be assigned to the O–W–O bending mode of bridging oxygen for $W_{18}O_{49}$. The characteristic Raman bands for $W_{18}O_{49}$ observed at 667 and 812 cm^{-1} are assigned to the asymmetric and symmetric stretching vibration modes of O–W–O, respectively. The Raman bands at 812 cm^{-1} can be attributed to the out-of-plane N–C–N bending of g-C_3N_4. This band at 920–1000 cm^{-1} corresponds to the W═O stretching vibration mode of a terminal oxygen and has been used as the characteristic shifts for $W_{18}O_{49}$ nanowires.[17] The intensity of this band was observed to decrease with increasing temperatures, due to the conversion of most of the $W_{18}O_{49}$ into WS_2. The disappearance of the 129, 225 and 667 cm^{-1} characteristic bands of β-WO_3 and $W_{18}O_{49}$, respectively, was observed for the WS_600 and WS_800 samples. As shown in Fig. 5b, additional bands were observed for WS_600 and WS_800 at 297, 350 and 416 cm^{-1} which corresponds to the E_{1g}, $E_{2g}{}^1$ and A_{1g} modes of WS_2, respectively. The $E_{2g}{}^1$ mode is linked to the in-plane, while A_{1g} mode correspond to out-of-plane phonon mode of WS_2. Additionally, the A_{1g} mode undergoes a slight red shift as the reaction temperature was increased from 600 to 800 °C. This shift triggered by the temperature increase is expected, due to the decrease in the interlayer van der Waals interaction resulting in weak restoring forces during lattice vibration. The BET surface area of the WS_2–g-C_3N_4 composites and pore size distribution of WS_600 is shown in Fig. S2 (ESI†). The resulting specific surface areas of WS_400, WS_600 and WS_800 was 61, 86 and 47 $m^2\ g^{-1}$, respectively. As shown in Fig. S2b (ESI†), WS_600 possesses mesopores with pore sizes of less than 37 nm which can facilitate efficient ion transport and accommodate the potential volume changes during the repeated charge–discharge processes.

As shown in Fig. 6, the chemical composition and valence state of the composites are characterized by XPS. The atomic percentage of all samples, with the calculated atomic ratios for N/C, pyridinic N [C–N–C]/pyrrolic N [N–$(C)_3$], W/S and WO_3/WS_2 are summarized in Table S1 (ESI†). The survey scan spectrum in

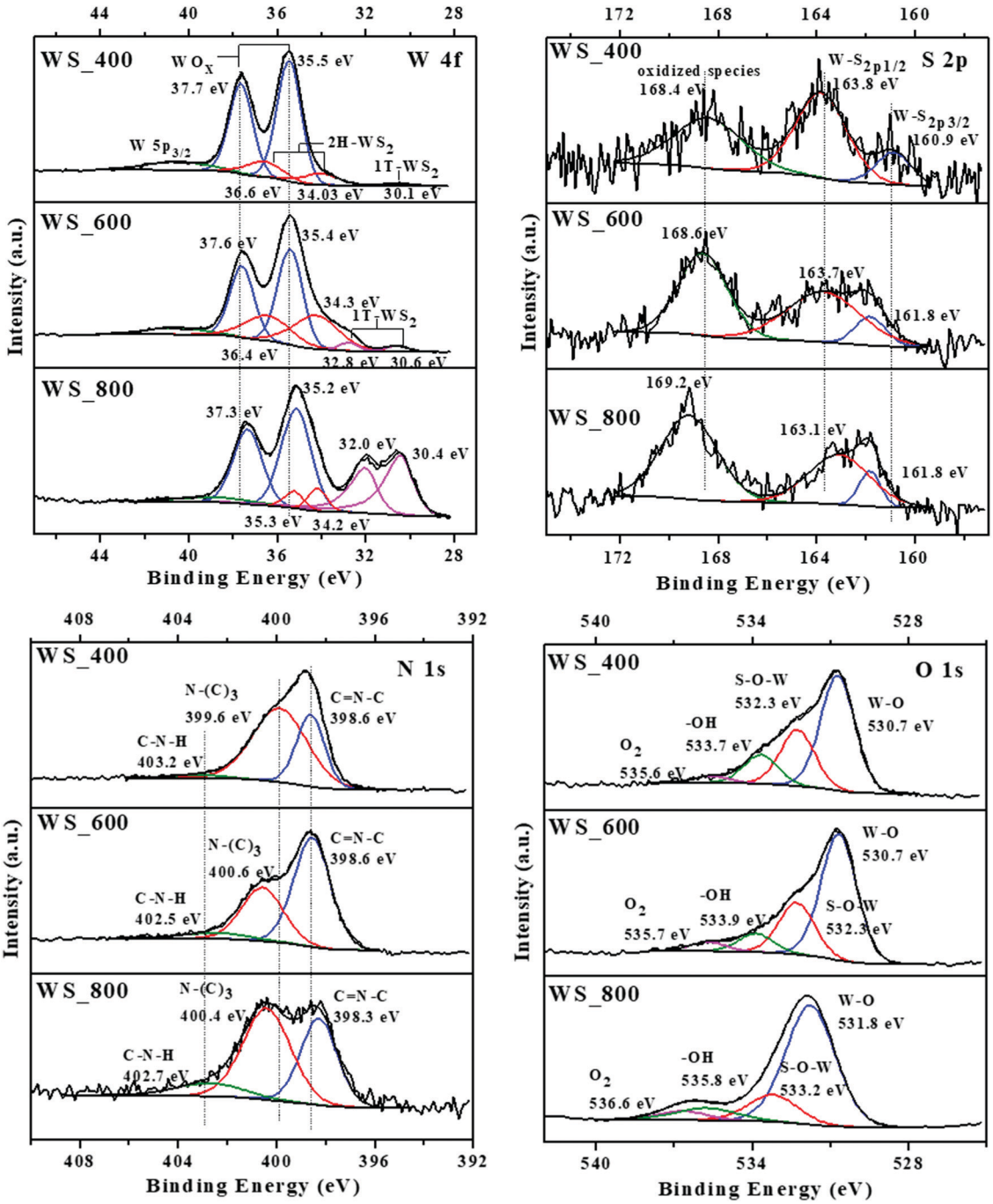

Fig. 6 High-resolution XPS spectra of W 4f, S 2p, N 1s and O 1s for all samples.

Fig. S2a (ESI†) confirms that C, N, O, W and S elements exist in WS_600. Considering the W 4f spectra of all samples, the binding energy at about 35 and 37 eV were generally attributed to W^{6+} species of tungsten oxide (WO_x). Two peaks of W $4f_{7/2}$ and W $4f_{5/2}$ at about 34 and 36 eV can be observed, indicating the semiconducting nature of the 2H phase WS_2. The peak locations are positively shifted to higher binding energies compared with the reference for 2H–WS_2 which is matched with the peak of W^{5+} in the WO_x structure.[18] However, the peak of one layer per (Trigonal) unit cell (1T) structure is observed in all samples. Together with the XRD results and TEM element mapping, these peaks are therefore assigned to 2 layers per hexagonal unit cell (2H)-phase of WS_2. The peak shift is linked to an incomplete transfer structure from WO_x to WS_2, and to the presence of W^{5+} species inside the WO_x structure.

The peaks at 30 and 32 eV can be attributed to metallic 1T–WS_2 structures or sulphur vacancies in the crystal structure,[19] which are present in both WS_600 and WS_800 samples. However, a shadow peak of the 1T phase WS_2 is also presented at 30.1 eV for WS_400 samples. The peak of W $5p_{3/2}$ at 40.5 eV is

attributed to the unavoidable surface oxidation of the samples. The S 2p spectra were deconvoluted into 3 peaks for all samples, which include S $2p_{3/2}$ peak at ~161 eV, S $2p_{1/2}$ peak at ~163 eV and the oxidized species at ~169 eV. The oxidised sulphate groups were generated from residues after reaction or intermediate products formed during the transformation of WS_2 from WO_x.[20] The peak percentage areas for both S $2p_{3/2}$ and S $2p_{1/2}$ in the sample decreased with increased temperature from 400 to 800 °C, *i.e.*, WS_400 to WS_800. As shown in Table S1 (ESI†), S content of the composites decreases with increasing calcination temperature. The same decreasing trend was observed for the atomic ratios of W to S, implying the absence of surface sulphur atoms Fig. 6.

The O 1s spectra of mixed WO_x/WS_2 nanostructures can be assigned into 4 peaks with binding energies of about 530, 532, 533 and 535 eV.[6] The peak at 530 eV is attributed to binding state of W^{6+} or W^{5+} corresponding to the lattice oxygen in WO_x; while the peak at 533 eV is from O_2 adsorbed on the WO_x/WS_2. The peak at 535 eV is assigned to OH-groups and water molecules, which can be chemisorbed on the defects and vacancies of the WO_x/WS_2 nanostructures. The peak at 322 eV can be associated with the O atom bonded to W atoms, which corresponded to S–O–W bonds indicating that an interfacial bond exists in the nanostructures.[21]

According to the high resolution XPS spectra of N 1s, three peaks at about 398, 399 and 402 eV correspond to the sp^2-bonded pyridinic N (C═N–C), pyrrolic N (N–$(C)_3$) groups and quaternary N (C–N–H), respectively.[22] The composites possess high N contents between 5.31 and 17 at%, showing that high N amounts are present in the final structures after calcination at 800 °C. As shown in Table S1 (ESI†), the N/C atomic ratio was observed to decrease from 0.24 to 0.065 with increasing calcination temperature. The same decreasing trend was observed for atomic ratios of pyridinic and pyrrolic N species where the atomic ratios decreased from 1.99 to 0.73 for WS_400 to WS_800, respectively. Conversely, an increasing trend was observed for the quaternary N (Fig. S4, ESI†). The decreasing N content can be linked to the introduction of N-vacancies while preferential loss of pyridinic N atoms over pyrrolic N atoms occurs due to unsaturated coordination which creates charge imbalance due to missing pyridinic N atoms.[23] The type and content of pyridinic, pyrrolic and quaternary N species have been reported to play a key role in influencing the structure (*i.e.*, defects and active sites) and electrochemical performance (*i.e.*, electron transport and conductivity).[7,23] As shown in Fig. S4 (ESI†), the WS_2–g-C_3N_4 composites possess a high content of pyridinic and pyrrolic N species, which can provide active sites for redox reactions, resulting in improved electrochemical performance.

As shown in Fig. S3b (ESI†), the core level spectrum of C 1s can be fitted with 4 peaks with positions around 284, 285, 287 and 290 eV, which are corresponding to the C–C, C–O/C–S, N═C–N and C–N bonds, respectively.[24] Therefore, all the structure analyses suggest that the WS_2–g-C_3N_4 composites contain mainly 2D WS_2 with residual amounts of WO_x. The amount of WS_2 (2H-phase) in the samples increased with the increases of temperature from 400 to 600 °C while the amount of WS_2 (2H-phase) in the 800 °C sample decreased, due to phase transformation of 2H to 1T. Overall, the total WO_3/WS_2 atomic ratio of the composites decreased with increased calcination temperature (Table S1, ESI†). The peaks of N and C confirmed the presence of graphitic carbon nitride within these samples.

Based on the XPS results, it is confirmed that WO_x/WS_2 was grown on the g-C_3N_4 surface and connected *via* van der Waals bonds. In addition, the 2H–WS_2 matrix contained S-vacancies due to WO_x–WS_x or 2H–1T phase transitions. This is supported by O 1s peak at about 322 eV), 1T (which can also refer to defects of WS_x structure) and oxidized species peaks from S 2p spectra.[25] Overall, the preferential bonding between the basal planes of WS_2 and g-C_3N_4 optimizes the electronic structure of the composite materials and activates the active sites.

3.2. Electrochemical performance evaluation

The electrochemical performance of the WS_2–g-C_3N_4 composites for supercapacitors was evaluated by using a three-electrode cell configuration in 0.5 M H_2SO_4 electrolyte. Fig. 7 and Fig. S5 (ESI†) show the electrochemical performance of the WS_2–g-C_3N_4 composites. As shown in Fig. 7a, Fig. S4a and c (ESI†), all WS_2–g-C_3N_4 composites possess a convex quasi-rectangular CV shape at potential windows of 0.2 to 1.0 V at various scan rates ranging from 10 to 100 mV s^{-1}, which is indicative of the pseudocapacitive behavior, due to the electric double layer capacitance (EDLC) and faradaic reactions of g-C_3N_4 and WS_2, respectively.

The shape of the well-defined CV curves is maintained at different scan rates, which indicates the capacity of the WS_2–g-C_3N_4 composites for fast charge transfer and improved rate performance. The galvanostatic charge/discharge profiles of WS_400, WS_600 and WS_800 electrodes at current densities between 2–15 A g^{-1} were measured and presented in Fig. 7b, Fig. S5b and d (ESI†), to evaluate the potential use of these composites as supercapacitors. The quasi-triangle shape of galvanostatic charge/discharge profiles is asymmetrical, suggesting the presence of some EDLC and faradaic reactions, which is consistent with the reported CV results. The WS_600 electrode exhibited a longer discharge time compared with other electrodes, supporting an optimal pseudocapacitive performance. The specific capacitance was calculated from the galvanostatic charge/discharge profiles of the WS_2–g-C_3N_4 electrodes, to highlight the rate capability which represents a measure of the charge and discharge capability of supercapacitors. The calculated specific capacitance values of WS_2–g-C_3N_4 electrodes at different current densities are shown in Fig. 7c. The electrodes of samples WS_400, WS_600 and WS_800 reveal specific capacitance values of 256, 1156 and 997 F g^{-1} when the N content was 17, 11.78 and 5.31 at%, respectively at a current density of 2 A g^{-1}. The specific capacitance values show that the nitrogen content must be kept around 11.78 at% to obtain optimal specific capacitance values. WS_600 electrode with N and S content of 11 at% and 1.01 at% had the maximum specific capacitance compared with other electrodes. Its specific capacitance remained as high as 832 F g^{-1} at a maximum current density of 15 A g^{-1}, due to its

excellent rate capability and electrochemical performance. In comparison, the specific capacitance values of WS_400 and WS_800 electrodes are 639 and 131 F g^{-1} at the same current density of 15 A g^{-1}. The specific capacitance retention of the WS_600 electrode was estimated to be 12.5% and 41% higher than those of WS_400 and WS_800, respectively, revealing the superior rate capability of WS_600 electrode. The specific capacitance of all the samples decreases with increasing current density due to the difficulty in ion transport at high current densities. In addition, the electrochemical stability was evaluated *via* cyclic galvanostatic measurements at a current density at 15 A g^{-1}. The stability of the WS_600 electrode over 10, 000 cycles at 15 A g^{-1} is shown in Fig. 7d. The WS_600 electrode exhibited excellent cyclic stability. After 10 000 cycles, the WS_600 electrode retained 82% of its initial specific capacitance. The specific capacitance of WS_600 is superior to the recently reported tungsten-based supercapacitors[26–32] (Table S2, ESI†). Overall, the WS_600 electrode possessed the optimal specific capacitance, improved rate capability and cyclic performance, against the WS_400 and WS_800 electrodes. The improved performance of WS_600 electrode is linked to the contributing effects of optimal surface area, surface defects (*i.e.*, sulfur vacancies in WS_2 and nitrogen vacancies in g-C_3N_4) as active sites, and both EDLC and redox reactions from the WS_2 and g-C_3N_4, which together facilitated the improved charge storage. The layered structures of WS_2 embedded in the g-C_3N_4 scaffold provided shorter pathways for a fast and efficient ion transport, while the porous feature could accommodate the potential volume changes during the repeated charge–discharge processes.

Besides utilization as supercapacitors, the WS_2–g-C_3N_4 composites also demonstrated interesting performance in hydrogen evolution reaction, which is a key process in the electrochemical water splitting. The electrocatalytic HER activities of the WS_2–g-C_3N_4 composites were evaluated using a three-electrode configuration in an acidic (0.5 M H_2SO_4) electrolyte, as shown in Fig. 8. The linear sweep voltammetry (LSV) curves of 20 wt% Pt/C and WS_2–g-C_3N_4 composites are displayed in Fig. 8a. The WS_600 electrode again showed a small onset potential of −0.06 V (*vs.* RHE) against other WS_2–g-C_3N_4 based electrodes, and was slightly higher than that of 20 wt% Pt/C. After which a sharp increase in the cathodic current was observed under negative potentials for all samples. The operating potential at a standard current density of 10 mA cm^{-2} was adopted in this study, for comparison purpose. This value is representative of the current density expected for a solar water splitting device operating at 12.3% efficiency.[33] WS_600 electrode exhibited excellent catalytic activity with a low overpotential of −0.170 V (*vs.* RHE) to drive a current density of 10 mA cm^{-2}.

In comparison, the WS_400 and WS_800 electrodes possessed higher overpotentials of −0.440 and −0.260 V (*vs.* RHE), respectively, to attain the same current density. These results affirmed the exceptional HER electrocatalytic activity of WS_600 amongst all samples.

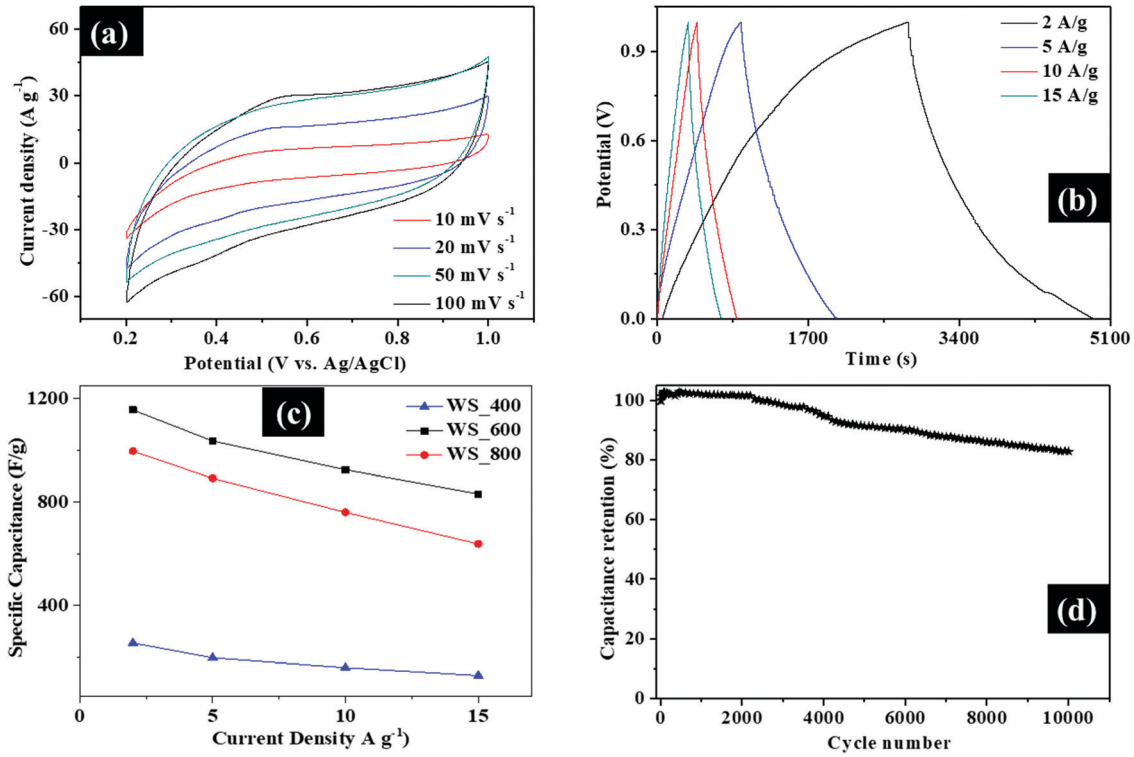

Fig. 7 (a) CV curves of the WS_600 electrode at various scan rates from 10 to 100 mV s^{-1}, (b) Galvanostatic charge discharge curves of WS_600 electrodes at different current densities, (c) Specific capacitance of WS_2–g-C_3N_4 composites as a function of current densities, and (d) Cyclic performance of WS_600 electrode at 15 A g^{-1}.

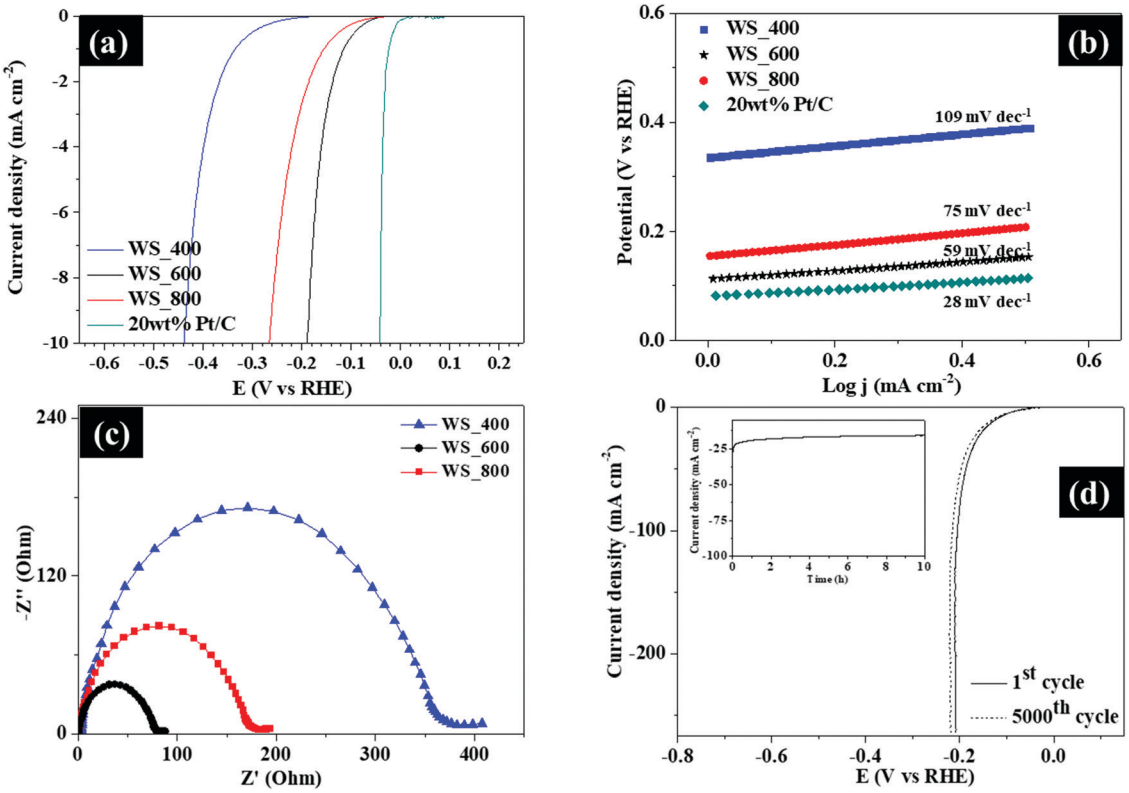

Fig. 8 (a) Polarization LSV curves, (b) Tafel plots, (c) EIS Nyquist plots and (d) LSV curves of WS_600 before and after cyclic studies (inset shows chronoamperometric measurements of WS_600).

The Tafel slopes of the samples were plotted to estimate the reaction kinetics and the rate-determining step for the HER process. As shown in Fig. 8b, the Tafel slope of WS_600 was 59 mV dec^{-1}, much lower than 75 and 109 mV dec^{-1} for WS_800 and WS_400, respectively, indicative of its faster kinetics. The low Tafel slope of WS_600 confirmed the favorable HER kinetics, which is linked to its layered structure providing more pathways for easy ion transportation. Hydrogen production for the samples was facilitated through a Volmer–Heyrovsky mechanism due to their Tafel slope values being within the range of 40 and 120 mv dec^{-1}, where electrochemical desorption and formation of hydrogen molecules occurred, respectively. The transition from the Volmer to Heyrovsky pathway is the rate limiting step for this mechanism. The excellent HER performance of WS_600 with low overpotential and Tafel slope is comparable to other previously reported tungsten-based electrodes in the literature[1,26,34–38] (Table S3, ESI†). The reaction kinetics occurring at the electrode/electrolyte interface was evaluated by EIS. Fig. 8c shows the Nyquist plots where the WS_2–g-C_3N_4 based electrodes showed semicircles at high frequency region, a little intercept at the real part and a line with large slope at low frequencies which is attributed to the charge transfer resistance (R_{ct}), intrinsic resistance (R_e), and the diffusion resistance (W), respectively. The WS_2–g-C_3N_4 based electrodes exhibit low resistance and fast ion transfer, which enhanced pseudocapacitance. The WS_600 exhibited a lower R_{ct} compared with other samples, due to better HER kinetics and enhanced ion transport at the electrode/electrolyte interface. The EIS plots of WS_600 before and after cycling (Fig. S6, ESI†) has a similar trend, where a slight increase of the R_{ct} and R_e was observed after 5000 cycles confirming the stability of WS_600.

The durability of WS_600 was investigated by cyclic linear potential sweeps and chronoamperometry measurements at the current density of 20 mA cm^{-2}. The polarization curve of WS_600 after continuous 5000 cycles at a scan rate of 5 mV s^{-1} exhibited only a small decay benchmarked against the initial cycle (Fig. 8d). The current–time curve showed that WS_600 was stabilized after 10 h with no attenuation in its current density. These observations indicated that the WS_600 possessed superior cyclic and long-term stability for the HER. Overall, the excellent electrochemical performance was attributed to WS_2–g-C_3N_4 composites, which provided more electroactive sites at electrolyte/electrocatalyst interface to facilitate effective ion transport and possessed ample active sites to allow intensive electrochemical reactions.

4. Conclusions

In summary, WS_2–g-C_3N_4 composites with surface vacancies were successfully prepared by using a facile solvothermal method followed by sulfidation. Experimental and computational studies revealed the preferential bonding and interfacial interaction

between the basal planes of WS_2 and g-C_3N_4, which optimizes the electronic structure, improves charge transfer and electrochemical performance. In comparison with other electrocatalysts, the WS_600 electrode showed excellent specific capacitance of 1156 F g^{-1} at the current density of 2 A g^{-1}, compared with 256 F g^{-1} for WS_400. The WS_600 electrode retained 82% of its initial specific capacitance after 10 000 cycles. In addition to demonstrating excellent specific capacitance, the WS_600 electrode also exhibited an excellent catalytic activity, with a low overpotential of 0.170 V (*vs.* RHE) capable of driving a current density of 10 mA cm^{-2} and a good stability after 8 h of testing. Overall, the WS_600 electrode possessed optimal specific capacitance, improved rate capability and cyclic performance, benchmarked against other samples due to the contributing effects of optimal specific surface area, surface defects (*i.e.*, sulfur vacancies in WS_2 and nitrogen vacancies in g-C_3N_4) as active sites, and both EDLC and redox reactions from the WS_2 and g-C_3N_4, which together facilitated the improved charge storage.

Conflicts of interest

There are no conflicts to declare.

Acknowledgements

This work was supported by the Leverhulme Trust Early Career Fellowship, ECF-2018-376.

References

1 B. Seo, *et al.*, Preferential horizontal growth of tungsten sulfide on carbon and insight into active sulfur sites for the hydrogen evolution reaction, *Nanoscale*, 2018, **10**, 3838–3848, DOI: 10.1039/C7NR08161H.
2 H. Jin, *et al.*, Colloidal single-layer quantum dots with lateral confinement effects on 2D exciton, *JACS*, 2016, **138**, 13253–13259, DOI: 10.1021/jacs.6b06972.
3 L. Wang, *et al.*, Coral-like-Structured Ni/C_3N_4 Composite Coating: An Active Electrocatalyst for Hydrogen Evolution Reaction in Alkaline Solution, *ACS Sustainable Chem. Eng.*, 2017, **5**, 7993–8003, DOI: 10.1021/acssuschemeng.7b01576.
4 D. Zheng, G. Zhang, Y. Hou and X. Wang, Layering MoS_2 on soft hollow g-C_3N_4 nanostructures for photocatalytic hydrogen evolution, *Appl. Catal., A*, 2016, **521**, 2–8, DOI: 10.1016/j.apcata.2015.10.037.
5 K. S. Lakhi, *et al.*, Mesoporous carbon nitrides: synthesis, functionalization, and applications, *Chem. Soc. Rev.*, 2017, **46**, 72–101.
6 J. Duan, *et al.*, Porous C3N4 nanolayers@N-graphene films as catalyst electrodes for highly efficient hydrogen evolution, *ACS Nano*, 2015, **9**, 931–940, DOI: 10.1021/nn506701x.
7 Q. Shen, *et al.*, Designing g-C_3N_4/N-rich carbon fiber composites for high-performance potassium-ion hybrid capacitors, *Energy Environ. Mater.*, 2020, **4**, 638–645, DOI: 10.1002/eem2.12148.
8 J. Wang, *et al.*, A defective g-C_3N_4/RGO/TiO_2 composite from hydrogen treatment for enhanced visible-light photocatalytic H_2 production, *Nanoscale*, 2020, **12**, 22030–22035, DOI: 10.1039/D0NR05141A.
9 H. J. Li, *et al.*, Sulfur vacancies in Co_9S_{8-x}/N-doped graphene enhancing the electrochemical kinetics for high-performance lithium–sulfur batteries, *J. Mater. Chem. A*, 2021, **9**, 10704–10713, DOI: 10.1039/D1TA00800E.
10 Y. Zhao, *et al.*, Preparation and characterization of tungsten oxynitride nanowires, *J. Mater. Chem.*, 2007, **17**, 4436–4440, DOI: 10.1039/B709486H.
11 J. Taylor, *et al.*, Theory of rectification in tour wires: The role of electrode coupling, *Phys. Rev. Lett.*, 2002, **89**, 138301, DOI: 10.1103/PhysRevLett.89.138301.
12 J. P. Perdew, *et al.*, Generalized gradient approximation made simple, *Phys. Rev. Lett.*, 1996, **77**, 3865, DOI: 10.1103/PhysRevLett.77.3865.
13 Y. Zhu, *et al.*, Catalytic activity origin and design principles of graphitic carbon nitride electrocatalysts for hydrogen evolution, *Front. Mater. Sci.*, 2019, **6**, 16, DOI: 10.3389/fmats.2019.00016.
14 A. Ghatak, *et al.*, Pulsed laser assisted growth of aligned nanowires of WO_3: role of interface with substrate, *RSC Adv.*, 2016, **6**, 31705–31716, DOI: 10.1039/C5RA27542C.
15 Y. Chen, *et al.*, Thin WS2 nanotubes from W18O49 nanowires, *Mater. Res. Lett.*, 2017, **5**, 508–515, DOI: 10.1080/21663831.2017.1337050.
16 O. Ola, *et al.*, DFT and experimental studies of iron oxide-based nanocomposites for efficient electrocatalysis, *J. Mater. Chem. C*, 2021, **9**, 6409–6417.
17 Z. Ma, *et al.*, Effects of WO_x modification on the activity, adsorption and redox properties of CeO_2 catalyst for NO_x reduction with ammonia, *J. Environ. Sci.*, 2012, **24**, 1305–1316.
18 A. Shpak, *et al.*, XPS studies of the surface of nanocrystalline tungsten disulfide, *J. Electron Spectrosc. Relat. Phenom.*, 2010, **181**, 234–238.
19 F. Perrozzi, *et al.*, Thermal stability of WS_2 flakes and gas sensing properties of WS_2/WO_3 composite to H_2, NH_3 and NO_2, *Sens. Actuators, B*, 2017, **243**, 812–822.
20 V. K. Singh, *et al.*, In situ functionalized fluorescent WS2-QDs as sensitive and selective probe for Fe^{3+} and a detailed study of its fluorescence quenching, *ACS Appl. Nano Mater.*, 2018, **2**, 566–576.
21 C. M. Smyth, *et al.*, WSe_2-contact metal interface chemistry and band alignment under high vacuum and ultra high vacuum deposition conditions, *2D Mater.*, 2017, **4**, 025084.
22 J.-W. Shi, *et al.*, Stable 1T-phase MoS_2 as an effective electron mediator promoting photocatalytic hydrogen production, *Nanoscale*, 2018, **10**, 9292–9303.
23 Z. Wang, *et al.*, Roles of N-vacancies over porous g-C_3N_4 microtubes during photocatalytic NO_x removal, *ACS Appl. Mater. Interfaces*, 2019, **11**, 10651–10662.
24 F. Wei, *et al.*, Oxygen self-doped g-C_3N_4 with tunable electronic band structure for unprecedentedly enhanced photocatalytic performance, *Nanoscale*, 2018, **10**, 4515–4522.

25 A. Ambrosi, *et al.*, 2H→ 1T phase transition and hydrogen evolution activity of MoS_2, $MoSe_2$, WS_2 and WSe_2 strongly depends on the MX_2 composition, *Chem. Commun.*, 2015, **51**, 8450–8453.
26 S. Hussain, *et al.*, One-Pot Synthesis of W_2C/WS_2 Hybrid Nanostructures for Improved Hydrogen Evolution Reactions and Supercapacitors, *Nanomaterials*, 2020, **10**, 1597.
27 L. Li, *et al.*, Hierarchical WS(2)@NiCo(2)O(4) Core-shell Heterostructure Arrays Supported on Carbon Cloth as High-Performance Electrodes for Symmetric Flexible Supercapacitors,'' (in eng), *ACS Omega*, 2020, **5**, 4657–4667, DOI: 10.1021/acsomega.9b04434.
28 Y. Li, *et al.*, Multifunctional porous nanohybrid based on graphene-like tungsten disulfide on poly(3,4-ethoxylenedioxythiophene) for supercapacitor and electrochemical nanosensing of quercetin, *J. Electrochem. Soc.*, 2020, **167**, 047512, DOI: 10.1149/1945-7111/ab721e.
29 W. Yin, *et al.*, Synthesis of tungsten disulfide quantum dots for high-performance supercapacitor electrodes, *J. Alloys Compd.*, 2019, **786**, 764–769, DOI: 10.1016/j.jallcom.2019.02.030.
30 X. Qiu, *et al.*, Immobilization of tungsten disulfide nanosheets on active carbon fibers as electrode materials for high performance quasi-solid-state asymmetric supercapacitors, *J. Mater. Chem. A*, 2018, **6**, 7835–7841, DOI: 10.1039/C8TA01047A.
31 F. Zheng, *et al.*, Novel diverse-structured h-WO_3 nanoflake arrays as electrode materials for high performance supercapacitors, *Electrochim. Acta*, 2020, **334**, 135641, DOI: 10.1016/j.electacta.2020.135641.
32 D. M. El-Gendy, *et al.*, Synthesis and characterization of WC@GNFs as an efficient supercapacitor electrode material in acidic medium, *Ceram. Int.*, 2020, **46**, 27437–27445, DOI: 10.1016/j.ceramint.2020.07.230.
33 X. Zou and Y. Zhang, Noble metal-free hydrogen evolution catalysts for water splitting, *Chem. Soc. Rev.*, 2015, **44**, 5148–5180, DOI: 10.1039/C4CS00448E.
34 Z. Huang, *et al.*, Polyoxometallates@zeolitic-imidazolate-framework derived bimetallic tungsten-cobalt sulfide/porous carbon nanocomposites as efficient bifunctional electrocatalysts for hydrogen and oxygen evolution, *Electro. Acta*, 2020, **330**, 135335, DOI: 10.1016/j.electacta.2019.135335.
35 T. P. Nguyen, *et al.*, Facile synthesis of WS_2 hollow spheres and their hydrogen evolution reaction performance, *Appl. Surf. Sci.*, 2020, **505**, 144574, DOI: 10.1016/j.apsusc.2019.144574.
36 J. Wu, *et al.*, Single-atom tungsten-doped CoP nanoarrays as a high-efficiency pH-universal catalyst for hydrogen evolution reaction, *ACS Sustainable Chem. Eng.*, 2020, **8**, 14825–14832, DOI: 10.1021/acssuschemeng.0c04322.
37 H. Tian, *et al.*, ''Oxygen vacancy-assisted hydrogen evolution reaction of the Pt/WO_3 electrocatalyst'', *J. Mater. Chem. A*, 2019, **7**, 6285–6293, DOI: 10.1039/C8TA12219A.
38 P. V. Sarma, *et al.*, Nanostructured Tungsten Oxysulfide as an Efficient Electrocatalyst for Hydrogen Evolution Reaction, *ACS Catal.*, 2020, **10**, 6753–6762, DOI: 10.1021/acscatal.9b04177.